HHS Public Access

Author manuscript

Nat Commun. Author manuscript; available in PMC 2014 December 25.

Published in final edited form as:

Nat Commun. ; 5: 4182. doi:10.1038/ncomms5182.

Self-assembled nanoscale coordination polymers with trigger release properties for effective anticancer therapy

Demin Liu, **Christopher Poon**, **Kuangda Lu**, **Chunbai He**, and **Wenbin Lin**

Department of Chemistry, University of Chicago, 929 E 57th Street, Chicago, IL 60637, USA

Wenbin Lin: wenbinlin@uchicago.edu

Abstract

Nanoscale coordination polymers (NCPs) are self-assembled from metal ions and organic bridging ligands, and can overcome many drawbacks of existing drug delivery systems by virtue of tunable compositions, sizes, and shapes; high drug loadings; ease of surface modification; and intrinsic biodegradability. Here we report the self-assembly of zinc bisphosphonate NCPs that carry 48±3 wt% cisplatin prodrug and 45±5 wt% oxaliplatin prodrug. *In vivo* pharmacokinetic studies in mice show minimal uptake of pegylated NCPs by the mononuclear phagocyte system and excellent blood circulation half-lives of 16.4±2.9 and 12.0±3.9 h for the NCPs carrying cisplatin and oxaliplatin, respectively. In all tumor xenograft models evaluated, including CT26 colon cancer, H460 lung cancer, and AsPC-1 pancreatic cancer, pegylated NCPs show superior potency and efficacy compared to free drugs. As the first example of using NCPs as nanotherapeutics with enhanced antitumor activities, this study establishes NCPs as a promising drug delivery platform for cancer therapy.

Introduction

Our understanding of cancer biology has progressed enormously in the past twenty years, [1] and yet mortality rates for many cancers have changed very little. The therapeutic **e**fficacy of many clinically used anticancer drugs, particularly conventional chemotherapeutics, is limited by their inability to preferentially accumulate in tumor tissues.[2, 3] Most chemotherapeutics are therefore administered at high doses in order to compensate for non-ideal biodistributions, which can lead to severe side effects.[4, 5] Such dose-limiting side effects prevent the complete eradication of cancer in a patient, thus allowing the recurrence of cancer and the development of drug resistance.[6, 7] For example, cisplatin is the most commonly used chemotherapeutic for treating testicular, lung, breast, bladder, ovarian, and head and neck cancers.[4, 8, 9] However, cisplatin causes numerous side effects, such as nephrotoxicity, which severely limit its clinical utility. Oxaliplatin was developed to treat gastric cancers, but its efficacy is also compromised by its dose limit toxicity, including

Author Contributions. W.L. and D.L. conceived the project. D.L., C.P., K.L., and C.H. performed the experiments and analyzed the results. D.L., C.H., and W.L. wrote the manuscript.

Conflict of Interest. The authors declare no competing financial interests.

peripheral neuropathy and neurotoxicity.[10] Therefore, the broader scientific and pharmaceutical community is in urgent need of novel strategies for selective delivery of chemotherapeutics to tumor tissues. Development of such strategies will lead to enhanced therapeutic efficacy that will directly benefit cancer patients.

Nanoparticles have recently emerged as a promising platform for the selective delivery of chemotherapeutics to cancer.[3, 11] Such nanotherapeutics can have prolonged blood circulation times to allow for preferential tumor accumulation by taking advantage of their enhanced permeation and retention in the leaky vasculatures of tumor tissues.[12] Over the past two decades, many nanoparticle platforms, including liposomes,[13-15] polymeric micelles,[16-18] organic polymers,[19-24] dendrimers,[25] metal and metal oxide,[26-28] and mesoporous silica[29-31] have been developed for the delivery of chemotherapeutics to cancer. These intensive studies have led to successful clinical translation of several nanotherapeutics since 1995, including doxorubicin (Doxil®), daunorubicin (Daunoxome®), amphotericin B (Ambisome®) and cytarabine (Depocyte®). However, optimal nanotherapeutics have yet to be developed because each of the existing delivery systems has its own limitations; for example, most of the clinically used nanotherapeutics are liposomal formulations, which are intrinsically less amenable to encapsulate hydrophilic drugs.

NCPs are constructed from metal-connecting points and organic bridging ligands via self-assembly processes.[32, 33] We believe that NCPs can combine the advantages of both organic nanoparticles, such as compositional tunability, biodegradability, and high drug loadings, and those of inorganic nanoparticles, such as well-defined particle morphologies and ease of surface functionalization, in order to afford an entirely new drug delivery platform. Although NCPs were previously examined as potential vehicles for delivering imaging agents and chemotherapeutics,[34-36] they have not yet been shown to be effective anticancer therapeutics *in vivo*.

Here we report the development of a novel, self-assembled zinc bisphosphonate NCP platform for the selective delivery of cisplatin and oxaliplatin to tumors. Two bisphosphonate ligands based on cisplatin and oxaliplatin prodrugs were used to construct robust NCPs with trigger release kinetics. The NCPs are pegylated to further stabilize the particles and to allow for long blood circulation times. Both NCP particles demonstrate enhanced antitumor activity when compared to free drugs in three different tumor xenograft models.

Results

Self-assembly and characterization of Zn bisphosphonate NCPs

Previously reported NCP-based nanotherapeutics use non-biocompatible metal ions and do not exhibit adequate stability for *in vivo* applications.[37, 38] There are recent reports on *in vivo* evaluations of NCPs, but the unfavorable pharmacokinetics and non-biocompatibility of these systems have greatly limited their applications *in vivo*.[39, 40] We explored Zn(II)-bisphosphonate NCPs in this work in order to enhance particle stability[41] and reduce excipient toxicity. Bisphosphonic acids containing cisplatin and oxaliplatin prodrugs, $\mathbf{L_1}$-H_4 and $\mathbf{L_2}$-H_4 (Fig. 1a), were synthesized by treating $Pt(NH_3)_2Cl_2(OH)_2$ and $Pt(dach)Cl_2(OH)_2$

(dach=*R, R*-diaminocyclohexane) with diethoxyphosphinyl isocyanate followed by deprotection of the phosphonate esters with bromotrimethylsilane (Supplementary Fig. 1-3 and Supplementary Methods).

Zn(II) bisphosphonate NCP containing the cisplatin prodrug, **1**, was prepared by vigorously stirring a mixture of $Zn(NO_3)_2$ and $\mathbf{L_1}$-Na_4 with 1,2-dioleoyl-sn-glycero-3-phosphate sodium salt (DOPA) in the Triton X-100/1-hexanol/cyclohexane/water reverse microemulsion at room temperature for 30 min. Transmission electron microscopy (TEM) images of **1** demonstrated the formation of uniform spherical nanoparticles with a diameter of 23.1±7.1 nm (Fig. 1b, Supplementary Fig. 4a and 5a), which matched the hydrodynamic diameter of 21.3±6.3 nm as measured by dynamic light scattering (DLS). Zn(II) bisphosphonate NCP containing the oxaliplatin prodrug, **2**, was similarly prepared by reacting $Zn(NO_3)_2$, $\mathbf{L_2}$-Na_4, and DOPA to afford slightly larger particles with a diameter of 26.9±10.7 nm by TEM (Fig. 1e, Supplementary Fig. 4d and 5c) and 28.7±9.2 nm by DLS (Fig. 1g). Prodrug loadings in **1** and **2** were determined by inductively coupled plasma-mass spectrometry (ICP-MS) to be 48±3 wt.% and 45±5 wt.%, respectively. DOPA-free **1** and **2** were also synthesized in order to determine DOPA amounts on the surface of NCP particles (Supplementary Fig. 6 and Supplementary Table 1). **1** and **2** are amorphous by powder X-ray diffraction, and have empirical formulae of $Zn_{3.5}\cdot\mathbf{L_1}\cdot DOPA_{0.3}\cdot(OH)_{2.7}\cdot 3H_2O$ and $Zn_{3.5}\cdot\mathbf{L_2}\cdot DOPA_{0.3}\cdot(OH)_{2.7}\cdot 5H_2O$ (Supplementary Fig. 7 and Supplementary Methods). The complete removal of Triton X-100 after washing was confirmed by high performance liquid chromatography (Supplementary Fig. 8).

NCPs **1** and **2** were further pegylated to afford **1P** and **2P** by mixing a tetrahydrofuran solution (0.276 mL) of 1,2-dioleoyl-sn-glycero-3-phosphocholine (DOPC, 0.54 umol), cholesterol (0.54 umol), and 1,2-distearoyl-sn-glycero-3-phosphoethanolamine-N-[methoxy(polyethylene glycol)-2000] (DSPE-PEG_{2k}, 0.27 umol) in a 4:4:2 molar ratio and NCP nanoparticles (0.5 mg) to 0.5 mL of 30% (v/v) ethanol/H_2O at 50 °C. This pegylation protocol takes advantage of the hydrophobic/hydrophobic interactions between DOPA and DOPC/cholesterol/DSPE-PEG_{2k} to form a self-assembled, asymmetric lipid bilayer on the NCP surface. Cholesterol is abundant in the membrane of animal cells at a molar concentration of 20-50%. The ability of cholesterol to order, condense, and stabilize a membrane structure has been extensively studied both experimentally and computationally.[42, 43]40 mol% cholesterol was added to the present formulations to stabilize the lipid bilayers. Upon evaporating tetrahydrofuran and cooling to room temperature, the particle suspension was used for cell and mouse studies. Although the TEM images did not show differences in size for the NCPs after pegylation, DLS measurements in 11.8 mM phosphate buffered saline (PBS) indicated that the hydrodynamic diameters of pegylated NCPs are 15-17 nm bigger than the particle diameters determined by TEM (Fig. 1c, 1f, Supplementary Fig. 4b, 4e,5b and 5d), which can be attributed to the lipid layer of DOPC/cholesterol/DSPE-PEG_{2k} on the particle surfaces as well as swelling of the NCP cores in PBS.[44] DLS diameters of **1**P and **2**P are 41.2±9.1 nm and 44.1±6.1 nm, respectively, and the ζ potentials measure neutral in PBS at pH=7.4 (Table 1). All of the synthetic steps have been scaled up to hundreds of milligram scales with standard laboratory glassware (500 mL), and the particles from hundreds of batches have shown consistent drug loadings, particle shapes

and sizes, and other characteristics, including ζ potential, particle stability, lipid coating and pegylation, and pharmacokinetic properties. The small sizes and near neutral ζ potentials of the pegylated NCPs make them excellent candidates for *in vivo* applications.[11, 45, 46] Pegylated Zn-pyrophosphate particles with a DLS diameter of 51.6±12.2 nm and a ζ potential of -1.2±0.7 mV were similarly synthesized (see Supplementary Fig. 9, Supplementary Table 2, and Supplementary Methods) and used as a control to test the safety of NCP particle excipients in animal studies.

Cytotoxicity of NCPs via endocytosis and triggered release

L_1 and **L_2** ligands are stable under typical physiological conditions, such as those circulating in the blood, but are expected to be readily reduced in more reducing environments, such as within tumor tissues and inside cancer cells. ^{195}Pt NMR studies indicated that **L_1** and **L_2** can be instantaneously reduced by 5 mM cysteine to afford cisplatin and oxaliplatin analog (Supplementary Fig. 10 and Supplementary Methods). The *in vitro* stability of **1P** and **2P** was evaluated in both PBS buffer with bovine serum albumin and PBS buffer supplemented with 10% fetal bovine serum (FBS) at 37 °C. Particle sizes remained unchanged over 20 h, thus showing the excellent colloidal and chemical stability of these particles (Supplementary Fig. 11 and Supplementary Methods). We also investigated the release kinetics of NCPs in cell culture medium supplemented with 10% FBS at 37 °C. The release kinetics is drastically different among lipid-coated, pegylated NCPs and bare particles (Supplementary Fig. 12). The release rate for **1P** and **2P** was significantly slowed down after pegylation and no burst release was observed, thus demonstrating the effectiveness of the coating strategy. Less than 10% of drug was released from **1P** and **2P** after incubation at 37 °C for 72 h, as compared to over 50% of drug release for the bare particles during the first 2h. The Zn release is faster than the drug release from **1P** and **2P**, probably due to the smaller sizes of Zn ions and thus more facile diffusion through the lipid membrane. The addition of 5 mM cysteine sped up the release of bare NCPs significantly, suggesting the ability to trigger the release of drugs via reductive degradation of NCPs. In contrast, cysteine did not enhance the drug release from **1P** and **2P**, presumably due to its inability to cross the lipid bilayer.

We hypothesized that NCPs can enter cancer cells via endocytosis and readily release cisplatin or oxaliplatin analog via reduction of **L_1** and **L_2** by intracellular reducing agents such as glutathione (Fig. 2a). In order to track the cell internalization of NCPs, we doped **1P** and **2P** with rhodamine B, an excellent optical imaging agent, by simply adding a small fraction of rhodamine B during the NCP synthesis to afford rhodamine B-doped **1P** (denoted as **1P′**) and **2P** (denoted as **2P′**) (Supplementary Fig. 13-15, Supplementary Table 3, and Supplementary Methods). Confocal laser scanning microscopy (CLSM) results showed that **1P** and **2P** (red fluorescence) were efficiently internalized into the cytoplasm of CT26 cells to induce cell apoptosis as evidenced by the TdT-mediated dUTP nick end labeling (TUNEL) assays (green fluorescence) (Fig. 2b, 2c, Supplementary Fig. 16, and Supplementary Methods). Furthermore, the presence of the characteristic DNA ladder in cells incubated with **1P**, cisplatin, cisplatin prodrug (**L_1**), **2P**, oxaliplatin, and oxaliplatin prodrug (**L_2**), rather than cells incubated with Zn Control, indicated that NCPs induced severe DNA damage and cell apoptosis with an efficiency similar to free drugs (Fig. 2d and Supplementary Methods). In line with the DNA ladder experiment results, cell viability

assays against CT26, H460, and AsPC-1 cancer cell lines gave similar IC_{50} values (inhibit cell growth by 50%) for NCPs when compared to their corresponding free drugs (Supplementary Fig. 17, Supplementary Table 4, and Supplementary Methods). Finally, we investigated the mechanisms involved in the internalization process by using several uptake inhibitors including chlorpromazine, genistein, methyl-β-cyclodextrin (Me- β-CD), wortmannin, and NaN_3(Supplementary Fig. 18 and Supplementary Methods). We also used Lysotracker Green to stain the endosomal/lysosomal compartments and Chlorea Toxin Subunit B (CT-B) to mark caveolae-mediated endocytosis (Supplementary Fig. 19 and Supplementary Methods). The results obtained from these experiments suggested that the internalization pathway of NCP particles was energy-dependent, clathrin-mediated, caveolae-mediated, and lipid-raft-mediated endocytosis rather than via macropinocytosis.

In vivo pharmacokinetic studies of pegylated NCPs

We conducted pharmacokinetic (pK) studies on **1P** and **2P** in order to determine their blood circulation profiles and biodistributions. The plasma Pt concentration (Cp) versus time data were fitted best by a one-compartment model with nonlinear elimination in both cases (Fig. 3). Circulation half-lives of **1P** and **2P** were determined to be 16.4±2.9 and 12.0±3.9 h, respectively (Table 2). Area under curves (AUCs) were more than 40-fold greater than the reported values of free cisplatin and oxaliplatin.[47, 48] The long circulation half-lives of **1P** and **2P** determined by Pt concentrations were consistent with those determined by Zn concentrations in the blood (Supplementary Fig. 20, 21, Supplementary Table 5, and Supplementary Discussion 1). Thus, **1P** and **2P** were cleared from the circulation much more slowly than their free drug counterparts.

We also performed pK studies on $\mathbf{L_1}$-H_4 and $\mathbf{L_2}$-H_4 as controls for **1P** and **2P**, respectively(Supplementary Fig. 22 and 23). There was significant amount of Pt in kidney and bladder for $\mathbf{L_1}$-H_4 and $\mathbf{L_2}$-H_4 at the 5 min time point, indicating the renal clearance of the prodrugs. A typical biphasic blood circulation profile was observed for both $\mathbf{L_1}$-H_4 and $\mathbf{L_2}$-H_4. The plasma Pt concentration versus time data were fitted best by a two-compartment model in both cases (Supplementary Fig. 22m and 23i). AUC values of $\mathbf{L_1}$-H_4 and $\mathbf{L_2}$-H_4 were estimated to be 10.8±3.1 and 13.4±2.5 μ g/ml×h, respectively, which are 70 and 22 times lower than those of **1P** (753±42.8 μg/ml×h) and **2P** (292±32.1 μg/ml×h), respectively(Supplementary Table 6).

In addition to slow plasma clearance, tissue distribution studies also showed that **1P** and **2P** were able to avoid uptake by the MPS, as judged by the low % ID/g (ID stands for injected dose) in liver, spleen, and kidney. This kind of biodistribution was not observed for non-pegylated NCPs. The pK study of non-pegylated **1** showed the deposition of significant amount of injected particles in liver and spleen (see Supplementary Fig. 22). In contrast, the majority of the injected dose of NCPs **1P** and **2P** remained in the blood after 24h, and tumor accumulation of the drug at the 24 h time-point approached 8.3±2.8 % ID/g for **1P** and 10.8±5.9 % ID/g for **2P**. In comparison, the highest value of tumor accumulation for non-pegylated **1** was only 1.2±2.8 %ID/g.

To further confirm the stability of NCPs in blood, we performed ultrafiltration on mice plasma samples obtained at 5 min and 1 h after intravenous (i.v.) injection of **1P** and **2P**. At the 5 min time point, the ultrafiltrates have 0.88±0.4%ID and 0.43±0.2% ID of Pt for **1P** and **2P**, respectively, as compared to 83.8±6.6% ID and 63.1±3.4% ID of Pt in the blood circulation for **1P** and **2P**, respectively. At the 60 min time point, the ultrafiltrates have 2.75±1.6% ID and 2.23±1.0% ID of Pt for **1P** and **2P**, respectively, as compared to 87.6±9.2% ID and 64.4±21.2% ID of Pt in the blood circulation for **1P** and **2P**, respectively (Supplementary Table 7 and Supplementary Methods). These results indicate that NCPs remain intact in blood circulation, with only a negligible amount of small molecule Pt drugs released in circulation. The NCPs thus possess exceptionally high drug loadings, ideal particle sizes and surface charges, excellent pharmacokinetics, and trigger release properties to make them excellent vehicles for the selective delivery of cisplatin and oxaliplatin to cancer cells *in vivo*.

In vivo toxicity

We examined the maximum tolerated dose (MTD) of **1P** and **2P** after a single i.v. injection to female Balb/c mice. The MTD was determined based on the group that all mice survived and did not lose over 20% weight. All mice received Zn Control at five times higher particle dose showed normal weight gain. Dose of **1P** at 3 mg/Kg and dose of **2P** at 8 mg/Kg were well tolerated by the mice, resulting in no death or over 20% weight loss. We conclude that the MTD is ≥3 mg/Kg for **1P** and ≥8 mg/Kg for **2P** (Supplementary Fig. 24 and Supplementary Methods).

In vivo efficacy studies of pegylated NCPs

Three tumor xenograft models, murine colon adenocarcinoma 26 (CT26), H460 human non-small cell lung cancer, and AsPC-1 human pancreatic cancer, were employed to assess the *in vivo* antitumor activity of pegylated NCPs. The CT26 colon cancer mouse model has been extensively used to study anticancer efficacy of liposomal and polymeric nanoparticles that carry cisplatin and oxaliplatin.[16, 47, 49] We further validated the anticancer activity of **1P** using subcutaneous mouse xenografts of the H460 cancer because cisplatin is the first-line treatment for non-small cell lung cancer in the clinic.[20, 50-52] Since oxaliplatin has showed promising results on pancreatic cancer in clinical trials, we used mouse subcutaneous xenografts of the AsPC-1 pancreatic cancer in order to ascertain the anticancer activity of **2P**.[16, 53-55]

Antitumor activity in CT26 cancer model

The antitumor activity of **1P** and **2P** was first evaluated on a CT26 tumor model. All doses were based on free cisplatin and oxaliplatin equivalents. CT26 tumor bearing mice were treated by i.v. injection of free cisplatin at the 3 mg/Kg dose or **1P** at doses of 0.75 mg/Kg or 0.5 mg/Kg every three days for three times (q3d×3). As shown in Fig. 4a, treatment with 0.75 mg/Kg of **1P** resulted in significantly higher antitumor activity (log growth rate of 0.21; P=0.0091) compared to treatment with free cisplatin at the 3 mg/Kg dose (log growth rate of 0.28). The antitumor efficacy of 0.5 mg/Kg of **1P** was also significantly higher (P=0.0002) when compared to the free cisplatin group. No differences were observed between the two

1P-treated groups (P>0.1). **1P** is thus at least six times more potent than free cisplatin in treating CT26 tumor-bearing mice.

We also determined the efficacy of **2P** on CT26 tumor-bearing mice. Mouse xenografts of CT26 tumor were treated intravenously with free oxaliplatin at the 5 mg/Kg dose or **2P** at the 2 mg/Kg dose four times every other day (q2d×4). The **2P**-treated group gave a log growth rate of 0.13, which was significantly more active (P=0.0002) than the oxaliplatin-treated group with a log growth rate of 0.26 (Fig. 5a).

The Kaplan-Meier survival plots of treated mice are shown in Fig. 4b and Fig. 5b and the results of the Log-rank tests are listed in Supplementary Table 8 whereas the median survival time (MST) and percentage increased life span (ILS (%)) for each treatment group are summarized in Supplementary Table 9. **1P**-treated mice showed an ILS of 29.4% and 36.8% compared to the control group. **2P** showed the largest survival benefit for CT26 tumor-bearing mice with an impressive ILS of 77.9%.

In all of the experiments, CT26 tumor-bearing mice were also injected with Zn Control particles at five times higher doses of Zn and lipid components. The Zn control particles did not lead to any tumor suppression, demonstrating the lack of cytotoxicity of the carrier components. Although an average weight loss of 5-10% was observed in NCP-treated groups on day 10^{th}, the mice quickly started to regain the weight once the treatments were finished. No significant difference in weight was observed between NCP and free drug treated groups at the end of these studies.

Antitumor activity in H460 cancer model

H460 tumor-bearing mice were treated with i.v. injections of free cisplatin at a 3 mg/Kg dose or **1P** at a 0.5 mg/Kg dose 3 times every 3 days (q3d×3). The **1P**-treated group gave a log growth rate of 0.10, which showed significantly greater tumor growth inhibition compared to free cisplatin that had a log growth rate of 0.16 (P =0.0048, Fig. 4c). No significant body weight loss was observed in mice over the course of this study (Supplementary Fig. 25). Photos of resected H460 tumors from various groups confirmed that **1P** significantly retarded tumor growth (Fig. 4d).

Antitumor activity in AsPC-1 cancer model

Subcutaneous AsPC-1 mouse xenografts were treated with i.v. injections of free oxaliplatin at a 5 mg/Kg dose or **2P** at a 2 mg/Kg dose 5 times every four days (q4d×5). The **2P**-treated group exhibited significantly higher tumor growth inhibition (with a log growth rate of 0.017) than the free oxaliplatin-treated group (with log growth rate of 0.036, P<0.001). Photos of resected AsPC-1 tumors from various groups confirmed the much enhanced tumor growth inhibition by **2P** over free oxaliplatin (Fig. 5d). Although ∼10% weight loss was observed for mice treated with **2P** after the fifth dose on day 18, these mice regained their weight once the treatment was finished. There was no significant difference in weight between **2P-** and free oxaliplatin-treated groups at the end of the study (Supplementary Fig. 25).

Histopathology analysis and blood chemistry of treated mice

Tumor growth inhibition curves and survival benefit analyses clearly indicate that pegylated NCPs are much more effective than their free drugs at treating subcutaneous (s.c.) xenografts of CT26, H460, and AsPC-1 cancers. Significantly higher tumor growth inhibition and survival benefits were achieved at 16% dose of **1P** and 40% dose of **2P** in terms of free drug equivalents. A histopathology analysis of the resected tumors confirmed the antitumor potency of NCP particles (Supplementary Fig. 26 and 27). Both the untreated and free drug-treated tumors were composed of large regions of viable tumor cells, while mice that received NCP nanoparticle treatment had tumors with much larger necrotic areas. In addition, no noticeable histopathological changes were observed for liver, kidney, lung, and spleen in mice treated with pegylated NCP particles (Supplementary Fig. 28 and 29), indicating a lack of general toxicity to normal tissues. The toxicity of the NCPs after 0.75 mg/Kg of **1P** q3d×3 and 2 mg/Kg of **2P** q2d×4 doses were quantitatively assessed further by examining mouse blood chemistry at 48h and 5 days after the last dose of treatment. No substantial changes of blood urea nitrogen, creatinine, aspartate aminotransferase, or alanine aminotransferase were observed during the time period and all values were within the normal range (Supplementary Table 10). Immunoglobulin E (IgE) levels, which are correlated with the hypersensitivity to platinum drugs, were also determined after chemotherapy. No significant difference was observed between mice treated with NCPs and mice treated with saline control (Supplementary Table 11 and Supplementary Methods).

NCP Tumor accumulation and *in vivo* apoptosis induction

Chlorin e6-doped NCPs were similarly synthesized (denoted as Ce6-**1P** and Ce6-**2P**) as **1P′** and **2P′**, and used for the imaging study (Supplementary Fig. 30 and 31, Supplementary Table 12, and Supplementary Methods). We conducted whole-body fluorescence imaging on CT26 tumor bearing mice with Ce6-**1P** in order to visualize and ascertain its enhanced tumor accumulation. When the tumor size reached around 100 mm^3, mice were intravenously injected with Ce6-**1P** at a dose equivalent to 6 mg/Kg cisplatin. Whole body imaging was performed before i.v. injection, 15min, 3h, 6h, 24h, 30h, and 48h after injection. A sustained systemic distribution of Ce6-**1P** was observed after particle injection, indicating the ability of Ce6-**1P** to effectively avoid particle opsonization and removal by the MPS. Furthermore, optical signals of tumors were clearly enhanced at 24 h and 48 h post injection (Fig. 6a). At the 24h time point, the fluorescence intensity of the tumor region is 8 times higher than that of pre-injection. The impressive passive targeting of tumors by Ce6-**1P** can thus be attributed to its prolonged circulation times, which significantly enhance the permeability and retention of the nanoparticles in tumors.

We also carried out CLSM imaging of dissected tumor tissues in order to ascertain the enhanced uptake of pegylated NCPs and induced apoptosis of cancer cells *in vivo*. 5-μm thick frozen sections of tumors were prepared and fixed with 4% (w/v) paraformaldehyde at 4 °C for 45 min. Tumor sections were stained with 4′,6-diamidino-2-phenylindole (DAPI) and marked by TUNEL. Significant fluorescence from chlorin e6 (red) and TUNEL (green) was observed in the confocal images (Fig. 6), indicating the ability of these particles to enter cancer cells and induce apoptosis *in vivo*. It is noted that the fluorescence signals from NCPs were uniformly distributed throughout the entire tumor section at 24 h post-injection,

suggesting deep tumor penetration of NCPs. In addition to deeper tumor penetration, the apoptosis signals can be seen in areas without particles, which was explained in a recent report to be a result of the “neighboring effect” which is unique to rapidly proliferating cancer cells such as CT26 cells.[56] The microdistributions of NCP particles in lung, spleen, liver, and kidney were also assessed at 24 h post-injection (Supplementary Fig. 32).

Discussion

Nanoparticles exhibit interesting properties that make them ideally suited for cancer imaging and drug delivery.[57] In particular, when compared to their small molecule counterparts, nanotherapeutics can have prolonged blood circulation times to allow for enhanced drug deposition in tumors by taking advantage of the enhanced permeability and retention (EPR) effect due to leaky vasculatures in tumor tissues.[12] However, most of the current nanoparticle platforms are either pure organic (such as liposomes, polymeric micelles, organic polymers, and dendrimers) or inorganic (such as metal, metal oxide, and mesoporous silica), and they each have strengths and weaknesses. We became interested in developing NCPs with the aim of combining strengths of both inorganic and organic systems into the same platform.[33, 58-61]

The advantages of using NCPs for drug delivery can be multi-fold. First, NCP formulations can provide unprecedentedly high drug loadings so minimum amounts of excipients are co-delivered to cancer cells. Second, the compositions, shapes, and sizes of the NCPs can be tuned by altering synthetic conditions to maximize their delivery efficiency. Third, NCPs are intrinsically biodegradable as a result of relatively labile metal-ligand bonds. Finally, the surface of NCPs can be further modified to impart biocompatibility and targeting efficacy.

As the surface properties of NCPs mostly dictate how they interact with cell milieus, proper surface chemistry needs to be employed to make NCPs a suitable drug delivery platform for cancer therapy in vivo. In this work, we used the well-established lipid-coating strategy to stabilize NCPs and to prolong their blood circulation times. Liposomes were first proposed as a drug delivery vehicle for cancer chemotherapy in 1974,[62] and this concept became a reality when the liposomes were further functionalized with a corona of polyethyleneglycol (PEG).[63] The hydrated PEG coating endows long circulating property to the liposomes by inhibiting protein adsorption and opsonization, leading to enhanced drug deposition in tumors via the EPR effect.[64] The NCP particles were synthesized in the presence of DOPA, and upon washing with EtOH and THF, afforded monodisperse particles with a monolayer of DOPA coating via Zn-phosphate interactions between NCPs and DOPA molecules and hydrophobic-hydrophobic interactions among DOPA molecules. The NCPs were further coated with DOPC, cholesterol, and DSPE-PEG_{2k} in a 4:4:2 molar ratio to lead to self-assembled, asymmetric lipid bilayers via hydrophobic/hydrophobic interactions between DOPA and DOPC/cholesterol/DSPE-PEG_{2k}. Importantly, the NCP core allows the use of a very high molar ratio (20 mol%) of DSPE-PEG_{2k} without destabilizing the lipid bilayer. In comparison, liposomes become unstable when the PEG molar ratios exceed 5mol %, and most of the currently developed or clinically used liposomes have ∼5mol % of PEG in lipid composition, including DOXIL,[65] SPI-77,[47] and Porphysome.[66] As a result of the PEG

coating at such a high molar ratio, NCPs **1P** and **2P** exhibit prolonged blood circulation times and enhanced deposition of the platin drugs in tumor tissues.

When compared to liposomal formulations such as SPI-77 and Lipoplatin, NCPs have much higher drug-to-lipid weight ratios of over 1:1. The drug-to-lipid weight ratio is 1: 70 for SPI-77 and 1:10 for Lipoplatin.[67] Despite its superior pharmacokinetic properties, SPI-77 did not demonstrate enhanced therapeutic efficacy over cisplatin in several tumor models due to the lack of cisplatin release in tumor tissue.[68, 69] As an example of polymer drug conjugates, ProLindac had a very high MTD of >250 mg/Kg in mice, but also suffered from poor drug release due to covalent attachment of the oxaliplatin prodrug to the polymer backbone.[48, 70] NCPs have similar particle sizes and drug loadings to polymeric micelle systems, such as CCDP/m and DACHPt/m, but are able to achieve comparable or better tumor inhibition by using much lower doses (0.5 mg/Kg of cisplatin and 2 mg/Kg of oxaliplatin for NCPs vs. 4 or 5 mg/Kg of cisplatin and 8 mg/Kg of oxaliplatin for polymeric micelle systems). This difference in performance can be attributed to the unique drug retention and release properties of NCPs. We hypothesize that upon endocytosis, **1P** and **2P** can lose some of the lipid coatings to expose bare NCP particles which will degrade to release cisplatin and oxaliplatin under reducing environments. Detailed comparisons of NCPs with selected formulations are summarized in Supplementary Table 13.

The three tumor models we examined in this work responded quite differently to cisplatin and oxaliplatin treatment. Colon cancer is more sensitive to oxaliplatin treatment than cisplatin treatment, thus the observed log growth rate of 0.13 after the treatment of **2P** is significantly slower than the growth rate of 0.21 obtained after the treatment of **1P**. Among the three models, CT26 is the most aggressive while AsPC-1 is the least aggressive. However, as pancreatic cancer is of the least permeable tumor, many attempts made to date to treat pancreatic cancer have failed. Only those particles with a small size to penetrate deeply into pancreatic tumor can elicit an antitumor effect. The *in vivo* results show that NCPs with a particle size of <50 nm are not only effective on highly permeable tumors like CT26 and H460, but also exert a high tumor growth inhibition effect on pancreatic tumor. This observation is consistent with the recent findings by Kataoka and coworkers.[16]

In summary, we have developed novel NCP-based nanotherapeutics that show significant and numerous advantages over existing systems. First, the self-assembly of NCPs is carried out under mild conditions without using specialized equipment, making the NCP synthesis highly scalable. Second, particle size and drug loading were found to be very consistent from batch to batch among the several hundreds of batches of NCP particles synthesized. Third, the NCP platform carries very high drug loadings, which not only minimizes the amount of excipients that are co-delivered but also alleviates the potential aggregation issue often encountered by particles with modest drug loadings. Fourth, a particle size of 30-50 nm and near neutral surface charge are two of the most desirable characteristics for nanotherapeutics. Small particles have enhanced penetration within tumors,[16] whereas particles with near neutral surface charge ranging (from -10 mV to +10 mV) can minimize nonspecific interactions with proteins, self-aggregation, and phagocytosis.[14] NCPs effectively avoid MPS uptakes to lead to long circulation times, which is a key prerequisite for passive targeting by the EPR effect. Fifth, we have shown that the excipients used in the

NCPs are non-toxic and biocompatible. Sixth, the pegylated NCPs showed no burst release at the initial stage, thus preventing premature drug release before the particles reach tumor sites. Finally, the NCP has a built-in trigger release mechanism to further enhance drug deposition in tumors.

With the above attributes, we have successfully demonstrated selective and substantial accumulation of chemotherapeutics with pegylated NCPs in solid tumors via the passive targeting pathways. In *in vivo* antitumor activity studies using CT26, H460, and AsPC-1 models, we showed that NCPs were significantly more effective than small molecule drugs even with 16.7% to 40% of the dose of free drugs. This level of enhanced potency is still rare in the nanomedicine literature, suggesting that NCPs represent a significant breakthrough as a novel and effective drug delivery system for potential translation to the clinic.

Methods

Materials

All of the starting materials were purchased from Aldrich and Fisher, unless otherwise noted, and used without further purification. 1,2-dioleoyl-sn-glycero-3-phosphocholine (DOPC), 1,2-dioleoyl-sn-glycero-3-phosphate sodium salt (DOPA), and 1,2-distearoyl-sn-glycero-3-phosphoethanolamine-N-[amino(polyethylene glycol) 2000] (DSPE-PEG_{2k}) were purchased from Avanti. Fetal bovine serum was purchased from Hyclone, Logan, UT. RPMI-1640 growth medium, penicillin-streptomycin, and phosphate buffered saline were bought from Gibco, Grand Island, NY. ^{1}H NMR spectra were recorded on a Bruker NMR 400 DRX Spectrometer at 400 MHz and referenced to the proton resonance resulting from incomplete deuteration of deuterated chloroform or dimethyl sulfoxide (DMSO). ^{195}Pt NMR spectra were referenced externally using standards of K_2PtCl_4 in D_2O (δ=-1628 ppm). UV-Vis absorption spectra were obtained using a Shimadzu UV-2401PC UV-Vis Spectrophotometer. Thermogravimetric analyses (TGA) were performed using a Shimadzu TGA-50 equipped with a platinum pan. A Hitachi 4700 field emission scanning electron microscope (SEM) and a JEM 100CX-II transmission electron microscope (TEM) were used to determine particle size and morphology. SEM images of the nanoparticles were taken on glass substrate. A Cressington 108 Auto Sputter Coater equipped with a Au/Pd (80/20) target and MTM-10 thickness monitor was used to coat the sample with approximately 5 nm of conductive layer before taking SEM images. Size and zeta potential data were collected with a Malvern Zetasizer Nano Zs. A Varian 820-MS Inductively Coupled Plasma-Mass Spectrometer was used to determine Mn and Pt concentration. Samples were introduced via a concentric glass nebulizer with a free aspiration rate of 0.4 mL/min, a Peltier-cooled double pass glass spraychamber, and a quartz torch. A peristaltic pump carried samples from a SPS3 autosampler (Varian) to the nebulizer. All standards and samples were in 2% HNO_3, prepared with MilliQ water. High performance liquid chromatography analysis of Triton X-100 was carried out on LC-10AT VP (Shimadzu, Japan) equipped with SPD-M10A VP diode array detector, SIL-10AF auto injector and SCL-10A VP system controller. Column: Dynamax-300A C18 (250×4.14 mm, 5 μm) (Rainin Instrument Co. InC., Woburn, MA).

Tumor model

Female, Foxn1$^{nu/nu}$ mice were inoculated subcutaneously with CT26 cells (1 million cells per mouse) or H460 cells (5 million cells per mouse) or AsPC-1 cells (5 million cells per mouse). Antitumor activity studies were performed when tumors were 30-50 mm^3 for CT26 and H460 and ~100 mm^3 for AsPC-1. Biodistribution studies were performed when the tumors were 100-200 mm^3. All animal experiments were performed in accordance with the protocol approved by the institutional animal care and use committee at the University of North Carolina and the University of Chicago.

Procedures for nanoparticle synthesis

A w=7.4 microemulsion was prepared by the addition of 0.2 mL of a 25 mg/mL **L$_1$**-Na$_4$ aqueous solution (obtained by deprotonation with 3M NaOH) and 0.2 mL of a 100 mg/mL $Zn(NO_3)_2$ aqueous solution to separate 5 mL aliquots of a 0.3 M Triton X-100/1.5 M 1-hexanol in cyclohexane mixture while vigorously stirring at room temperature. 20 uL of DOPA solution (200 mg/mL in $CHCl_3$) was added to the complex solution and the stirring was continued for 15 min until a clear solution formed. The two microemulsions were combined, and the resultant 10 mL microemulsion with w=7.4 was stirred for 30 minutes. After the addition of 20 mL ethanol, **1** was obtained by centrifugation at 12000 rpm. The resulting pellet was washed once with ethanol and twice with 50% EtOH/THF, and redispersed in THF. Particles were purified by filtration through 200 nm syringe filter. **2** was similarly prepared.

General procedures for pegylation

Pegylated particles were obtained by adding a THF solution of DOPC, cholesterol (1:1molar ratio), DSPE-PEG$_{2k}$ (20 mol%) and nanoparticles to 500 μl 30% (v/v) EtOH/H_2O at 50 °C. THF was completely evaporated and the solution was allowed to cool to room temperature before use.

Pharmacokinetics and tissue distributions

Mice were injected in the right flank with 1 million CT26 cells and tumors were allowed to grow until 100 to 200 mm^3 before they received a 3mg cisplatin or oxaliplatin/kg dose of NCP particles by tail vein injection. Animals were sacrificed (3 per time-point) at 5min, 1h, 3h, 8h, 24h, and 48h after dosing. Liver, lung, spleen, kidney, and bladder were excised and kept in dry ice before analysis. Blood was collected by cardiac puncture and kept in heparinized tubes. Organs and blood were digested in concentrated nitric acid for at least 24h and analyzed by ICP-MS.

In vivo antitumor activity

CT26 cells (1 million cells per mouse), H460 cells (5 million cells per mouse), or AsPC-1 (5 million cells per mouse) were injected subcutaneously into the right flank of mice. Tumor volume and body weights were measured for individual animals three times weekly in all experiments. Tumor volume was determined by measuring the tumor in two dimensions with calipers and calculated using the formula tumor volume = (length×width^2)/2. Mice were sacrificed when tumor volume reached the maximum allowed size. Median survival

time (MST (day)) was defined as the time at which half of the mice had died. The percentage increased life span (ILS (%)) was calculated using the following equation: ILS (%) = [(MST of treated group /MST of control group)-1] × 100.

Tissue histopathology evaluation

Liver, kidney, and tumors were received in a formalin solution. For histology, organs and tumors were placed in labeled cassettes and flushed with water for 20 min. Samples were then transported to the Lineberger Comprehensive Cancer Center Animal Histopathology Core Lab in a 70% ethanol solution where they were pariffinized, cut, and hematoxylin and eosin (H&E) stained. The stained samples were imaged at the UNC Microscopy Services Laboratory using an Olympus BX61 Upright Fluorescence Microscope equipped with Improvision's Volocity software. Images were captured using a QImaging RETIGA 4000R color camera.

Blood chemistry analysis

To test hepatic and renal functions of treated mice, blood was drawn 48 h and 5 days after the last dose of treatment for blood chemistry analyses. Blood samples were centrifuged down at 6000 rpm for 15 min, and the supernatant blood serums were collected and transported to UNC Animal Clinical Laboratory Core Facility for analysis of creatine (CRT), blood urea nitrogen (BUN), alanine aminotransferase (ALT), and aspartate aminotransferase (AST) levels using Vitros 350 Chemistry System (Ortho Clinical Diagnostics Company, Rochester, NY).

In vivo fluorescence imaging

CT26 cells were injected subcutaneously into the right flank of female nude mice. When the tumor size reached around 100 mm^3, mice were intravenously injected with **1P**'. Whole body imaging was performed under the IVIS Kinetic Imaging System (Caliper Life Sciences, Hopkiton, MA) with excitation filter of 640 nm and emission filter of 700 nm before i.v. injection, 15min, 3h, 6h, 24h, 30h, and 48h after injection. All imaging parameters were kept constant for the whole imaging study. Binning factor = 4, exposure time = 3 sec, f number = 2, field of view = 12.5. Region of interest (ROI) values were recorded using Living Image® software as total photon counts per centimeter squared per steradian ($p/s/cm^2/sr$).

Confocal Microscopy

Tumor was harvested, rinsed in saline, and cryofixed in OCT medium. Frozen sections of 5-μm thick were prepared and fixed with 4% (w/v) paraformaldehyde at 4 °C for 45 min. To visualize cell apoptosis, TdT-mediated dUTP nick end labeling (TUNEL) reaction was performed on tumor sections using DNA fragmentation detection kit (Life Technology, USA) according to the manufacturer's instructions. The nuclei were stained with 10 ug/mL of 4′,6-diamidino-2-phenylindole (DAPI). Images were captured with an Olympus Fluoview 1000 confocal laser scanning microscope (CLSM) at the University of Chicago Integrated Light Microscopy Facility.

Statistical analysis

The SAS statistical package (SAS, Institute, Inc., Cary, NC) was used for longitudinal data and repeated measurement analysis. SAS procedure PROC MIXED with unspecified covariance structure was used to evaluate treatment and time effects on tumor growth. We fitted mixed models to the tumor growth curve data by a log transformation of tumor volume at each time point and estimated the exponential growth rates. Survival studies were analyzed using the Kaplan-Meier and Log-rank tests with Origin.

Supplementary Material

Refer to Web version on PubMed Central for supplementary material.

Acknowledgments

We acknowledge National Cancer Institute (U01–CA151455) for funding support. We thank Andrew Z. Wang for helpful discussions and Ms. Charlene Santos and Mr. Jimmy Pan for their help in animal studies.

References

1. Umar A, Dunn BK, Greenwald P. Future directions in cancer prevention. Nat Rev Cancer. 2012; 12:835–848. [PubMed: 23151603]
2. Torchilin V. Tumor delivery of macromolecular drugs based on the EPR effect. Adv Drug Del Rev. 2011; 63:131–135.
3. Jain RK, Stylianopoulos T. Delivering nanomedicine to solid tumors. Nat Rev Clin Oncol. 2010; 7:653–664. [PubMed: 20838415]
4. Kelland L. The resurgence of platinum-based cancer chemotherapy. Nat Rev Cancer. 2007; 7:573–584. [PubMed: 17625587]
5. Davis ME, Chen Z, Shin DM. Nanoparticle therapeutics: an emerging treatment modality for cancer. Nat Rev Drug Discov. 2008; 7:771–782. [PubMed: 18758474]
6. Piddock LJV. Multidrug-resistance efflux pumps ? not just for resistance. Nat Rev Micro. 2006; 4:629–636.
7. Higgins CF. Multiple molecular mechanisms for multidrug resistance transporters. Nature. 2007; 446:749–757. [PubMed: 17429392]
8. Jung Y, Lippard SJ. Direct Cellular Responses to Platinum-Induced DNA Damage. Chem Rev. 2007; 107:1387–1407. [PubMed: 17455916]
9. Wang D, Lippard SJ. Cellular processing of platinum anticancer drugs. Nat Rev Drug Discov. 2005; 4:307–320. [PubMed: 15789122]
10. Qi XL, et al. A flexible metal azolate framework with drastic luminescence response toward solvent vapors and carbon dioxide. Chem Sci. 2011; 2:2214–2218.
11. Wang AZ, Langer RS, Farokhzad OC. Nanoparticle Delivery of Cancer Drugs. Annu Rev Med. 2011; 63:185–198. [PubMed: 21888516]
12. Maeda H, Sawa T, Konno T. Mechanism of tumor-targeted delivery of macromolecular drugs, including the EPR effect in solid tumor and clinical overview of the prototype polymeric drug SMANCS. J Controlled Release. 2001; 74:47–61.
13. Allen TM, Cullis PR. Liposomal drug delivery systems: From concept to clinical applications. Adv Drug Del Rev. 2013; 65:36–48.
14. Davis ME. The First Targeted Delivery of siRNA in Humans via a Self-Assembling, Cyclodextrin Polymer-Based Nanoparticle: From Concept to Clinic. Mol Pham. 2009; 6:659–668.
15. Torchilin VP. Recent advances with liposomes as pharmaceutical carriers. Nat Rev Drug Discov. 2005; 4:145–160. [PubMed: 15688077]

16. Cabral H, et al. Accumulation of sub-100 nm polymeric micelles in poorly permeable tumours depends on size. Nat Nanotechnol. 2011; 6:815–823. [PubMed: 22020122]
17. Murakami M, et al. Improving Drug Potency and Efficacy by Nanocarrier-Mediated Subcellular Targeting. Sci Transl Med. 2011; 3:64ra62.
18. Siddik Z, Jones M, Boxall F, Harrap K. Comparative distribution and excretion of carboplatin and cisplatin in mice. Cancer Chemother Pharmacol. 1988; 21:19–24. [PubMed: 3277732]
19. Schluep T, et al. Preclinical Efficacy of the Camptothecin-Polymer Conjugate IT-101 in Multiple Cancer Models. Clin Cancer Res. 2006; 12:1606–1614. [PubMed: 16533788]
20. Peng XH, et al. Targeted Delivery of Cisplatin to Lung Cancer Using ScFvEGFR-Heparin-Cisplatin Nanoparticles. ACS Nano. 2011; 5:9480–9493. [PubMed: 22032622]
21. Dhar S, Kolishetti N, Lippard SJ, Farokhzad OC. Targeted delivery of a cisplatin prodrug for safer and more effective prostate cancer therapy in vivo. Proc Natl Acad Sci. 2011; 108:1850–1855. [PubMed: 21233423]
22. Cabral H, Nishiyama N, Okazaki S, Koyama H, Kataoka K. Preparation and biological properties of dichloro(1,2-diaminocyclohexane)platinum(II) (DACHPt)-loaded polymeric micelles. J Controlled Release. 2005; 101:223–232.
23. Fu K, Pack D, Klibanov A, Langer R. Visual Evidence of Acidic Environment Within Degrading Poly(lactic-co-glycolic acid) (PLGA) Microspheres. Pharm Res. 2000; 17:100–106. [PubMed: 10714616]
24. Dhar S, Gu FX, Langer R, Farokhzad OC, Lippard SJ. Targeted delivery of cisplatin to prostate cancer cells by aptamer functionalized Pt(IV) prodrug-PLGA–PEG nanoparticles. Proc Natl Acad Sci. 2008; 105:17356–17361. [PubMed: 18978032]
25. Bosman AW, Janssen HM, Meijer EW. About Dendrimers:,Äâ Structure, Physical Properties, and Applications. Chem Rev. 1999; 99:1665–1688. [PubMed: 11849007]
26. Cobley CM, Chen J, Cho EC, Wang LV, Xia Y. Gold nanostructures: a class of multifunctional materials for biomedical applications. Chem Soc Rev. 2011; 40:44–56. [PubMed: 20818451]
27. Kim J, Piao Y, Hyeon T. Multifunctional nanostructured materials for multimodal imaging, and simultaneous imaging and therapy. Chem Soc Rev. 2009; 38:372–390. [PubMed: 19169455]
28. Cabral H, Nishiyama N, Kataoka K. Optimization of (1,2-diamino-cyclohexane)platinum(II)-loaded polymeric micelles directed to improved tumor targeting and enhanced antitumor activity. J Controlled Release. 2007; 121:146–155.
29. Ashley CE, et al. The targeted delivery of multicomponent cargos to cancer cells by nanoporous particle-supported lipid bilayers. Nat Mater. 2011; 10:389–397. [PubMed: 21499315]
30. Maeda H. Tumor-Selective Delivery of Macromolecular Drugs via the EPR Effect: Background and Future Prospects. Bioconjug Chem. 2010; 21:797–802. [PubMed: 20397686]
31. Lu J, Liong M, Zink JI, Tamanoi F. Mesoporous Silica Nanoparticles as a Delivery System for Hydrophobic Anticancer Drugs. Small. 2007; 3:1341–1346. [PubMed: 17566138]
32. Oh M, Mirkin CA. Chemically tailorable colloidal particles from infinite coordination polymers. Nature. 2005; 438:651–654. [PubMed: 16319888]
33. Lin W, Rieter WJ, Taylor KML. Modular Synthesis of Functional Nanoscale Coordination Polymers. Angew Chem Int Ed. 2009; 48:650–658.
34. Horcajada P, et al. Porous metal-organic-framework nanoscale carriers as a potential platform for drug delivery and imaging. Nat Mater. 2010; 9:172–178. [PubMed: 20010827]
35. Rieter WJ, Pott KM, Taylor KM, Lin W. Nanoscale coordination polymers for platinum-based anticancer drug delivery. J Am Chem Soc. 2008; 130:11584–11585. [PubMed: 18686947]
36. Taylor-Pashow KML, Della Rocca J, Xie Z, Tran S, Lin W. Postsynthetic Modifications of Iron-Carboxylate Nanoscale Metal-Organic Frameworks for Imaging and Drug Delivery. J Am Chem Soc. 2009; 131:14261–14263. [PubMed: 19807179]
37. Huxford-Phillips RC, Russell SR, Liu D, Lin W. Lipid-coated nanoscale coordination polymers for targeted cisplatin delivery. RSC Adv. 2013; 3:14438–14443. [PubMed: 24058727]
38. Rieter WJ, Pott KM, Taylor KML, Lin W. Nanoscale Coordination Polymers for Platinum-Based Anticancer Drug Delivery. J Am Chem Soc. 2008; 130:11584–11585. [PubMed: 18686947]

39. Baati T, et al. In depth analysis of the in vivo toxicity of nanoparticles of porous iron(iii) metal-organic frameworks. Chem Sci. 2013; 4:1597–1607.
40. Lim CK, et al. Gadolinium-coordinated elastic nanogels for in¬†vivo tumor targeting and imaging. Biomaterials. 2013; 34:6846–6852. [PubMed: 23777911]
41. Gagnon KJ, Perry HP, Clearfield A. Conventional and Unconventional Metal-Organic Frameworks Based on Phosphonate Ligands: MOFs and UMOFs. Chem Rev. 2012; 112:1034–1054. [PubMed: 22126609]
42. Weis RM, McConnell HM. Cholesterol stabilizes the crystal-liquid interface in phospholipid monolayers. J Phys Chem. 1985; 89:4453–4459.
43. Wennberg CL, van der Spoel D, Hub JS. Large Influence of Cholesterol on Solute Partitioning into Lipid Membranes. J Am Chem Soc. 2012; 134:5351–5361. [PubMed: 22372465]
44. Xia X, et al. Quantifying the Coverage Density of Poly(ethylene glycol) Chains on the Surface of Gold Nanostructures. ACS Nano. 2011; 6:512–522. [PubMed: 22148912]
45. Alexis F, Pridgen E, Molnar LK, Farokhzad OC. Factors Affecting the Clearance and Biodistribution of Polymeric Nanoparticles. Mol Pham. 2008; 5:505–515.
46. Dreher MR, et al. Tumor Vascular Permeability, Accumulation, and Penetration of Macromolecular Drug Carriers. J Natl Cancer Inst. 2006; 98:335–344. [PubMed: 16507830]
47. Newman MS, Colbern GT, Working PK, Engbers C, Amantea MA. Comparative pharmacokinetics, tissue distribution, and therapeutic effectiveness of cisplatin encapsulated in long-circulating, pegylated liposomes (SPI-077) in tumor-bearing mice. Cancer Chemother Pharmacol. 1999; 43:1–7. [PubMed: 9923534]
48. Rice JR, Gerberich JL, Nowotnik DP, Howell SB. Preclinical Efficacy and Pharmacokinetics of AP5346, A Novel Diaminocyclohexane-Platinum Tumor-Targeting Drug Delivery System. Clin Cancer Res. 2006; 12:2248–2254. [PubMed: 16609041]
49. Nishiyama N, et al. Novel Cisplatin-Incorporated Polymeric Micelles Can Eradicate Solid Tumors in Mice. Cancer Res. 2003; 63:8977–8983. [PubMed: 14695216]
50. White SC, et al. Phase II study of SPI-77 (sterically stabilised liposomal cisplatin) in advanced non-small-cell lung cancer. Br J Cancer. 2006; 95:822–828. [PubMed: 16969346]
51. Furuse K, et al. Phase III Study of Concurrent Versus Sequential Thoracic Radiotherapy in Combination With Mitomycin, Vindesine, and Cisplatin in Unresectable Stage III Non,ÄìSmall-Cell Lung Cancer. J Clin Oncol. 1999; 17:2692. [PubMed: 10561343]
52. Scagliotti GV, et al. Phase III Study Comparing Cisplatin Plus Gemcitabine With Cisplatin Plus Pemetrexed in Chemotherapy-Naive Patients With Advanced-Stage Non,ÄìSmall-Cell Lung Cancer. J Clin Oncol. 2008; 26:3543–3551. [PubMed: 18506025]
53. Stathopoulos GP, Boulikas T, Kourvetaris A, Stathopoulos J. Liposomal Oxaliplatin in the Treatment of Advanced Cancer: A Phase I Study. Anticancer Res. 2006; 26:1489–1493. [PubMed: 16619562]
54. Xiong HQ, et al. Phase 2 trial of oxaliplatin plus capecitabine (XELOX) as second-line therapy for patients with advanced pancreatic cancer. Cancer. 2008; 113:2046–2052. [PubMed: 18756532]
55. Alberts SR, et al. Gemcitabine and oxaliplatin for metastatic pancreatic adenocarcinoma: a North Central Cancer Treatment Group phase II study. Ann Oncol. 2003; 14:580–585. [PubMed: 12649105]
56. Guo S, et al. Lipid-Coated Cisplatin Nanoparticles Induce Neighboring Effect and Exhibit Enhanced Anticancer Efficacy. ACS Nano. 2013; 7:9896–9904. [PubMed: 24083505]
57. Doane TL, Burda C. The unique role of nanoparticles in nanomedicine: imaging, drug delivery and therapy. Chem Soc Rev. 2012; 41:2885–2911. [PubMed: 22286540]
58. Liu D, et al. Coercing bisphosphonates to kill cancer cells with nanoscale coordination polymers. Chem Commun. 2012; 48:2668–2670.
59. Huxford RC, deKrafft KE, Boyle WS, Liu D, Lin W. Lipid-coated nanoscale coordination polymers for targeted delivery of antifolates to cancer cells. Chem Sci. 2012; 3:198–204.
60. Liu D, Huxford RC, Lin W. Phosphorescent Nanoscale Coordination Polymers as Contrast Agents for Optical Imaging. Angew Chem Int Ed. 2011; 50:3696–3700.

61. deKrafft KE, et al. Iodinated Nanoscale Coordination Polymers as Potential Contrast Agents for Computed Tomography. Angew Chem Int Ed. 2009; 48:9901–9904.
62. Gregoriadis G, Swain CP, Wills EJ, Tavill AS. DRUG-CARRIER POTENTIAL OF LIPOSOMES IN CANCER CHEMOTHERAPY. The Lancet. 1974; 303:1313–1316.
63. Klibanov AL, Maruyama K, Torchilin VP, Huang L. Amphipathic polyethyleneglycols effectively prolong the circulation time of liposomes. FEBS Lett. 1990; 268:235–237. [PubMed: 2384160]
64. Andresen TL, Jensen SS, Jørgensen K. Advanced strategies in liposomal cancer therapy: Problems and prospects of active and tumor specific drug release. Prog Lipid Res. 2005; 44:68–97. [PubMed: 15748655]
65. Barenholz Y. Doxil® — The first FDA-approved nano-drug: Lessons learned. J Controlled Release. 2012; 160:117–134.
66. Lovell JF, et al. Porphysome nanovesicles generated by porphyrin bilayers for use as multimodal biophotonic contrast agents. Nat Mater. 2011; 10:324–332. [PubMed: 21423187]
67. Boulikas T. Clinical overview on Lipoplatin™: a successful liposomal formulation of cisplatin. Expert Opin Investig Drugs. 2009; 18:1197–1218.
68. Bandak S, Goren D, Horowitz A, Tzemach D, Gabizon A. Pharmacological studies of cisplatin encapsulated in long-circulating liposomes in mouse tumor models. Anti-cancer drugs. 1999; 10:911–920. [PubMed: 10630359]
69. Zamboni W, et al. Systemic and tumor disposition of platinum after administration of cisplatin or STEALTH liposomal-cisplatin formulations (SPI-077 and SPI-077 B103) in a preclinical tumor model of melanoma. Cancer Chemother Pharmacol. 2004; 53:329–336. [PubMed: 14673619]
70. Nollwotnik DP, Cvitkovic E. ProLindac,Ñ¢ (AP5346): A review of the development of an HPMA DACH platinum Polymer Therapeutic. Adv Drug Del Rev. 2009; 61:1214–1219.

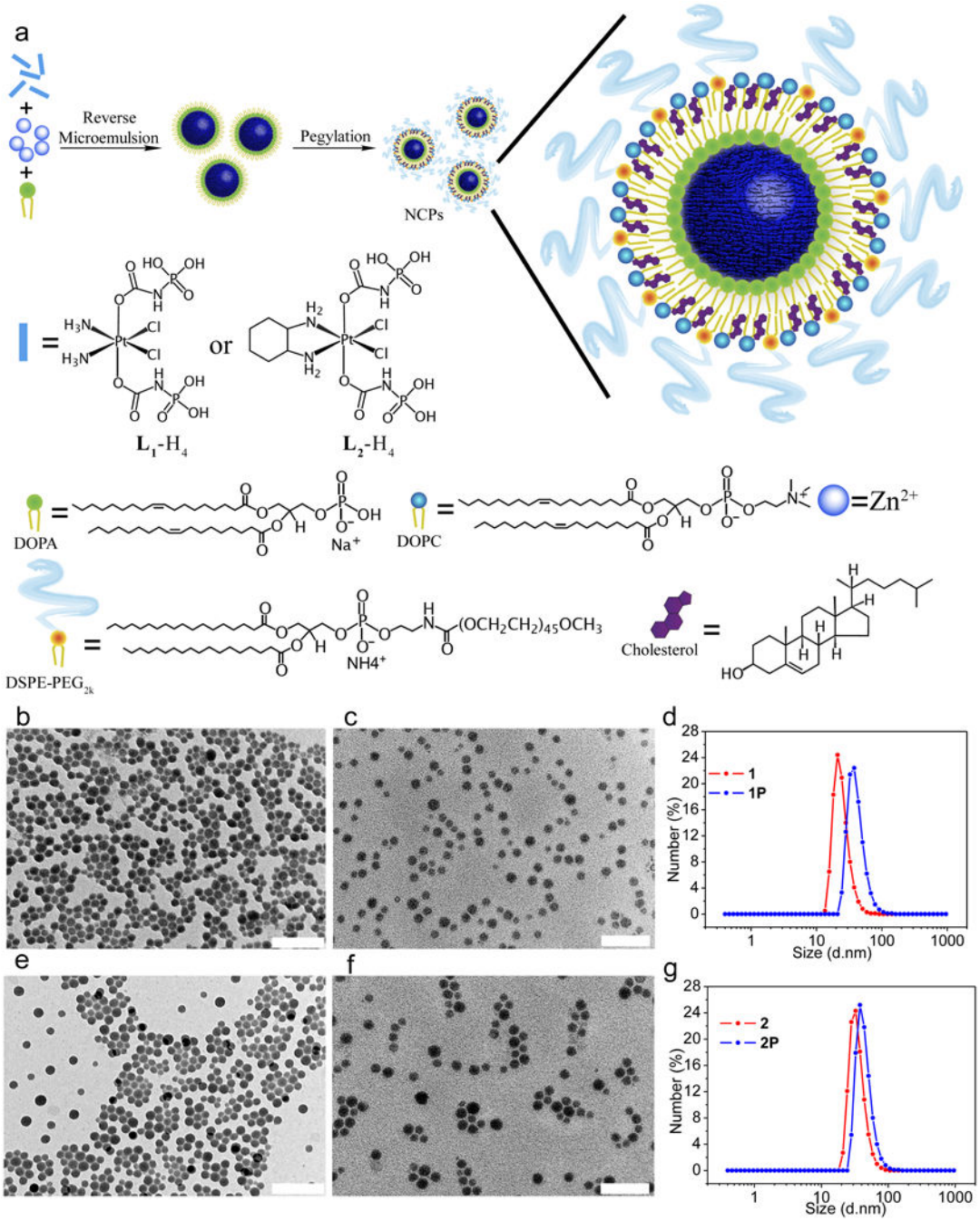

Figure 1. Schematic illustration and TEM images of NCPs

(a) General procedure for self-assembly of NCPs with lipid and PEG coatings. TEM images of (b) **1**; (c) **1P**; (e) **2**. (f) **2P**. Size distribution of **1** (d) and **2** (g) measured by dynamic light scattering. Scale bars = 100 nm.

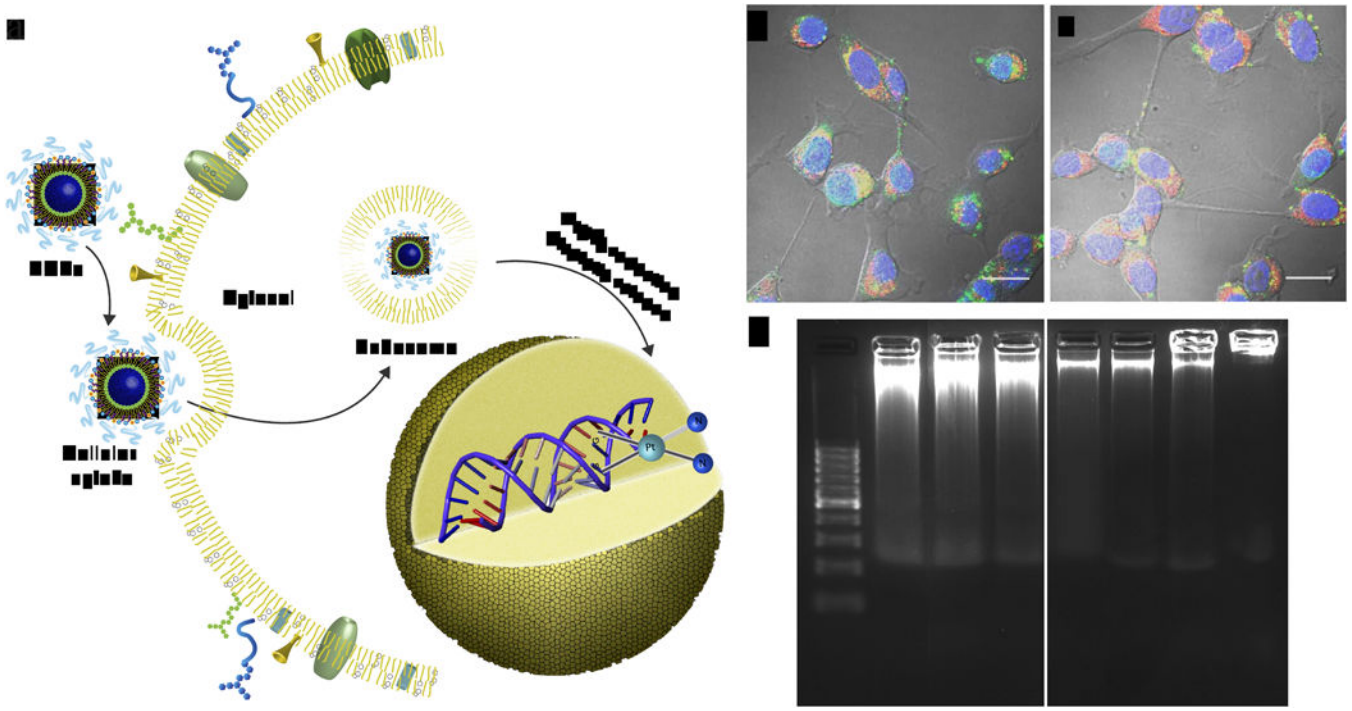

Figure 2. Proposed uptake pathways of NCPs and the mechanism of action

(a) Schematic showing endocytosis of NCPs and subsequent reduction of $\mathbf{L_1}$ or $\mathbf{L_2}$ by intracellular reducing agents, such as glutathione, to release cytotoxic cisplatin and oxaliplatin. (b) Confocal fluorescence images of CT26 cells incubated with **1P′** (b) and **2P′** (c), showing particle internalization (red channel) and cell apoptosis (green channel). Scale bars = 20 μm. The orange color is due to the overlap of red and green color. (d) Gel electrophoresis images showing DNA damage induced by NCPs. From left to right: DNA marker, **1P**, cisplatin, cisplatin prodrug, **2P**, oxaliplatin, oxaliplatin prodrug, and Zn Control.

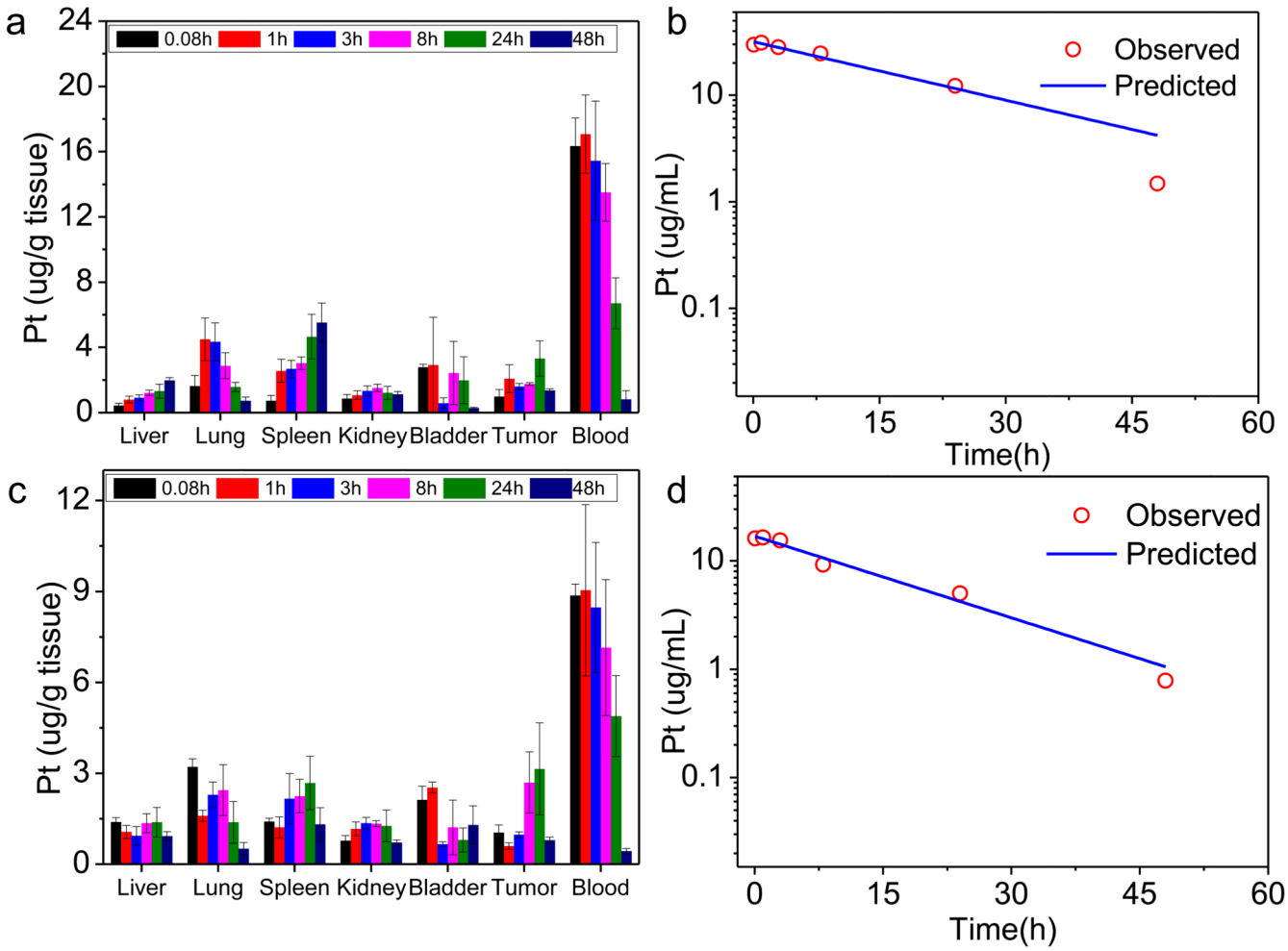

Figure 3. Pharmocokinetic and tissue distribution studies of NCPs

Tissue distributions of **1P** (a) and **2P (c)** at time points of 5 min, 1 h, 3 h, 8 h, 24 h, and 48 h after i.v. injection of corresponding nanoparticles. Data are expressed as means±SD (n=3). Observed and fitted time-dependent Pt concentrations in plasma following **1P** (b) and **2P** (d) administration.

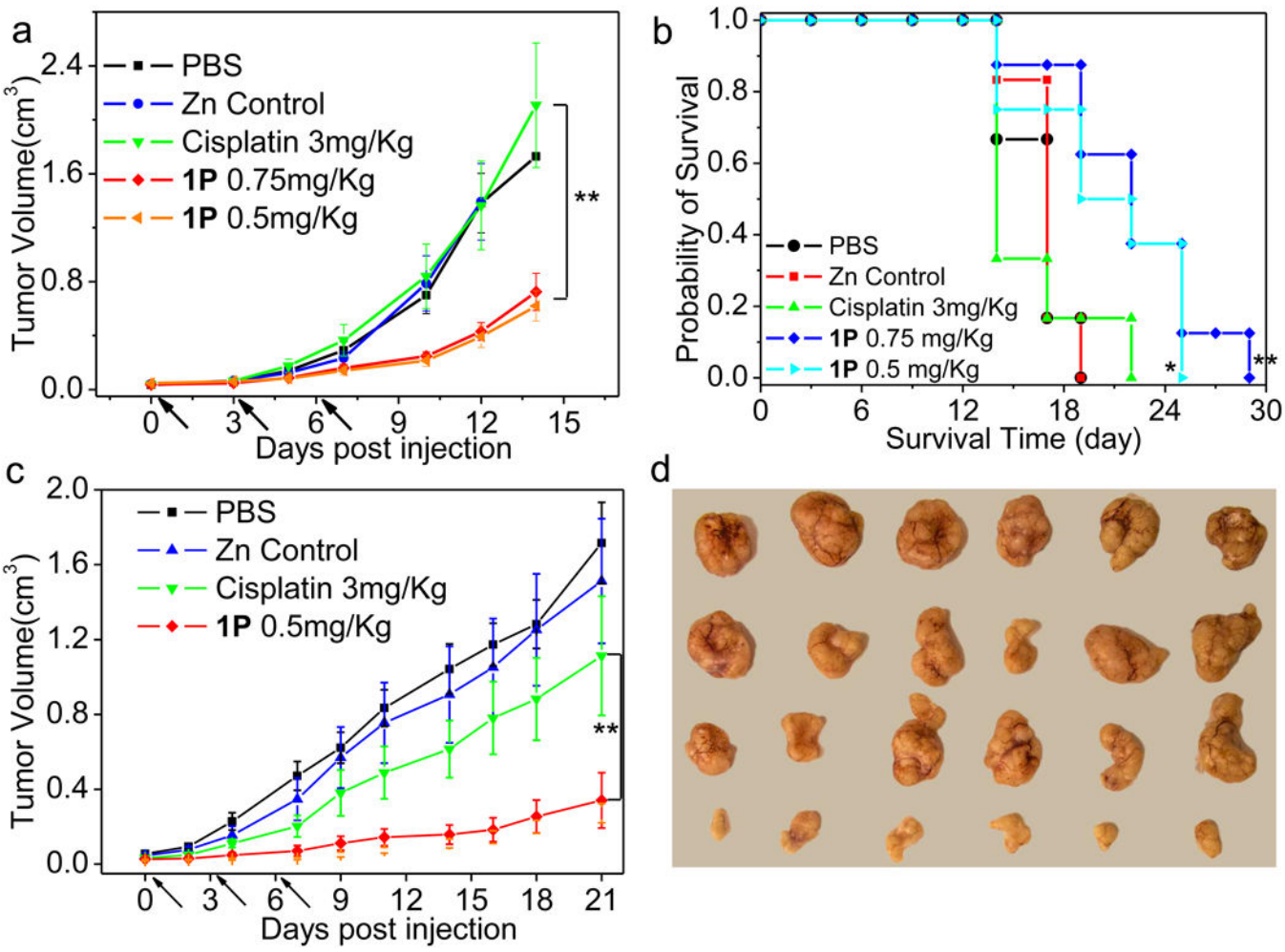

Figure 4. ***In vivo*** **antitumor activity evaluation of 1P**

(a) *In vivo* tumor growth inhibition curves for PBS, Zn Control, free cisplatin and **1P** on the subcutaneous C26 tumor model. Cisplatin (dose, 3 mg/Kg) and **1P** (dose, 0.75 mg/Kg or 0.5 mg/Kg) were administered on day 0, 3, 6. (b) Kaplan-Meier plots showing the percentage of animals remaining in the study with the subcutaneous C26 tumor model. (c) *In vivo* tumor growth inhibition curves for PBS, Zn Control, free cisplatin and **1P** on the subcutaneous H460 tumor model. Cisplatin (dose, 3mg/Kg) and **1P** (dose, 0.5mg/Kg) were administered on day 0, 3, 6. Data are expressed as means±SEM (n=6-8), *p<0.05, **p<0.01, ***p<0.001. (d) Photos of resected H460 tumors from various groups. From top to bottom: PBS, Zn Control, free cisplatin, and **1P**.

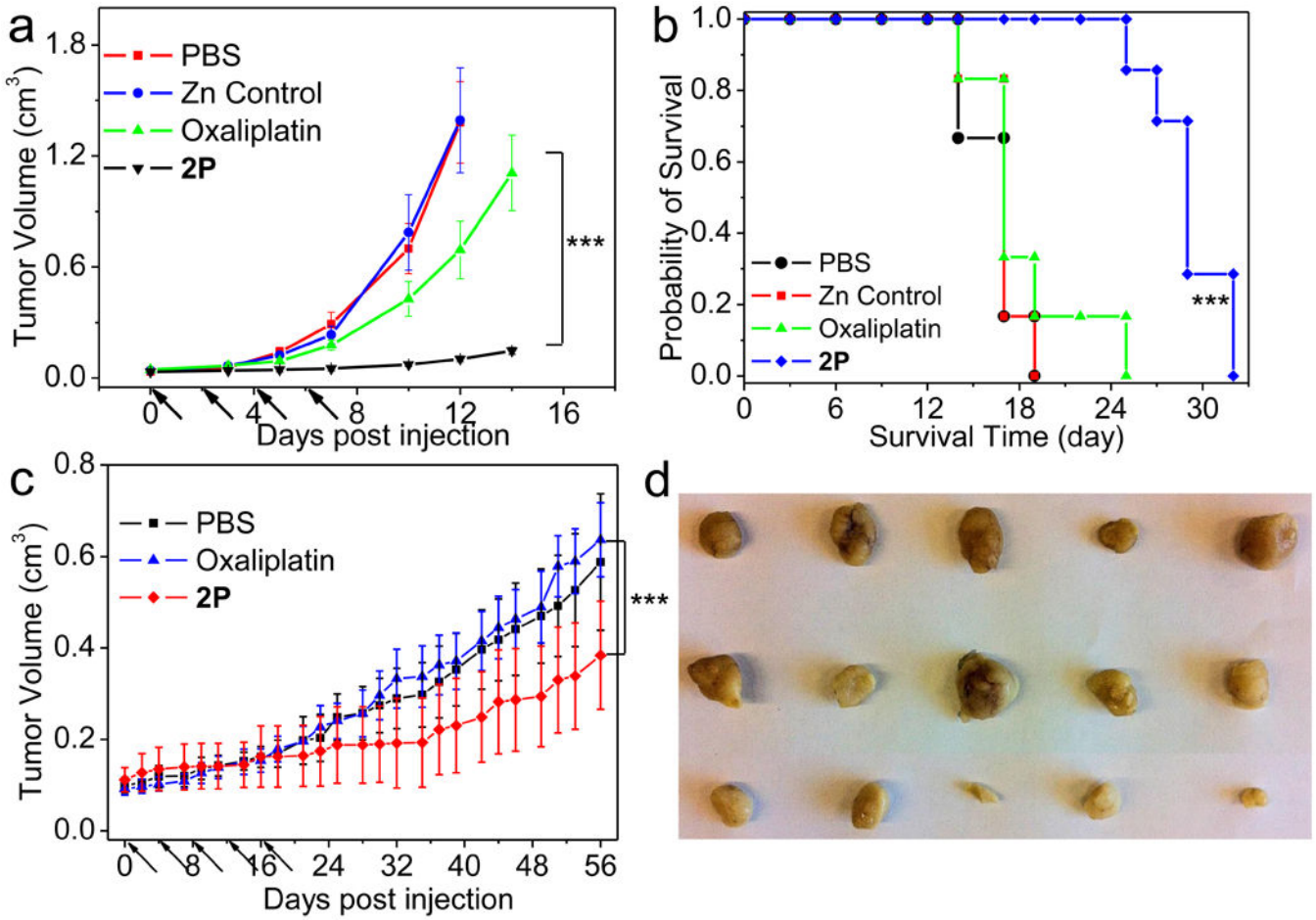

Figure 5. ***In vivo*** **antitumor activity evaluation of 2P**

(a) *In vivo* tumor growth inhibition curves for PBS, Zn Control, oxaliplatin and **2P** on the subcutaneous C26 tumor model. Oxaliplatin (dose, 5mg/Kg) and **2P** (dose, 2mg/Kg) were administered on day 0, 2, 4, 6. (b) Kaplan-Meier plots showing the percentage of animals remaining in the study with the subcutaneous C26 tumor model. (c) *In vivo* tumor growth inhibition curves for PBS, free oxaliplatin and **2P** on the subcutaneous AsPC-1 tumor model. Oxaliplatin (dose, 5 mg/Kg) and **2P** (dose, 2 mg/Kg) were administered on day 0, 4, 8, 12, 16. Data are expressed as means±SEM (n=5-8), *p<0.05, **p<0.01, ***p<0.001. (d) Photos of resected AsPC-1 tumors from various groups. From top to bottom: PBS, Oxaliplatin, and **2P**.

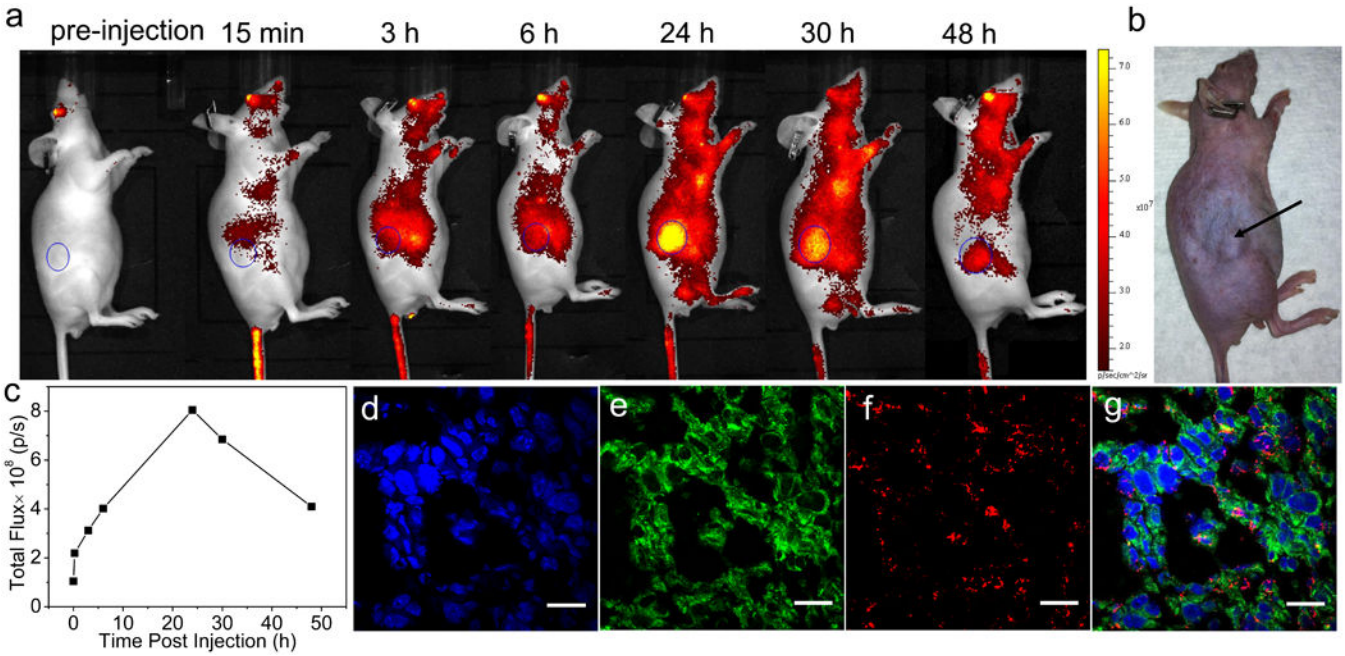

Figure 6. ***In vivo*** **fluorescence imaging**

(a) Time-dependent fluorescence images of CT26 tumor bearing mouse showing increasing tumor contrast due to the accumulation of **1P′** inside the tumor. (b) Digital camera image of the same mouse showing the tumor position. (c) Measurements of the fluorescence intensity of the tumor region (circular ROIs shown in (a)). (d)-(g) are confocal fluorescence images of CT26 tumor cells. Channels are: DAPI nuclear stain (blue), apoptosis by TUNEL assays (green), and Chlorin e6 from the particles (red). Scale bars = 20 μm.

Table 1

Physicochemical properties of NCPs.

NCPs	TEM diameter (nm)	Number-Ave diameter (nm)	PDI*	ζ Potential (mV)
1	23.1±7.1	21.3±6.3#	0.11	NA
1P	24.2±8.4	41.2±9.1$	0.14	-0.9±0.5
2	26.9±10.7	28.7±9.2#	0.15	NA
2P	28.9±7.6	44.1±6.1$	0.13	-1.0±0.6

*Polydispersity index.

#Measured in THF.

$Measured in PBS buffer.

Data are expressed as means±SD.

Table 2

Pharmacokinetic parameters for NCPs in CT26 colon tumor bearing mice.*

NCP	C_0 (μg/ml)	k_0 (1/h)	V_{ss} (mg/kg/(μg/ml))	Cl ((mg/kg)/(μg/ml)/h)	AUC (μg/ml×h)	MRT (h)	$t_{1/2}$ (h)
1P	31.7±3.7	0.042±0.005	0.06±0.007	0.003±0.0004	753.1±42.8	23.7±4.2	16.4±2.9
2P	16.9±4.9	0.058±0.017	0.09±0.025	0.005±0.0016	292.4±32.1	17.3±5.6	12.0±3.9

*Parameters used to describe this model are: C_0, plasma concentration at time=0; k_0, elimination rate constant; $t_{1/2}$, the time required to reduce the plasma concentration to one half its initial value; V, volume of distribution; V_{SS}, volume of distribution at steady state; Cl, systemic clearance, AUC, total area under curve; MRT, mean resident time (time for 63.2% of the administered dose to be eliminated).